applied sciences

MDPI

Article

Oxidation Behaviour of Refractory $(HfCo)_{100-x}(NbMo)_x$ High-Entropy Alloys with a bcc+B2 Structure

Nikita Yurchenko [1,2], Evgeniya Panina [1,2], Sergey Zherebtsov [1,2] and Nikita Stepanov [1,2,*]

1 Laboratory of Bulk Nanostructured Materials, Belgorod National Research University, Belgorod 308015, Russia; yurchenko_nikita@bsu.edu.ru (N.Y.); panina_e@bsu.edu.ru (E.P.); zherebtsov@bsu.edu.ru (S.Z.)

2 World-Class Research Center "Advanced Digital Technologies", State Marine Technical University, Saint Petersburg 198095, Russia

* Correspondence: stepanov@bsu.edu.ru

Abstract: Herein, the oxidation behaviour of refractory $(HfCo)_{100-x}(NbMo)_x$ (x = 0; 10; 25; 40; 75; 100 (at.%)) high-entropy alloys with a bcc+B2 structure subjected to cyclic oxidation at 1000 °C was studied. The single-phase B2-ordered HfCo alloy demonstrated the best spallation resistance and retained a pristine form after 100 h. The oxidation kinetics of the HfCo alloy was near-parabolic, accompanied by the formation of external HfO_2 or CoO layers after 1 or 100 h, respectively. Additions of $(NbMo)_x$ deteriorated the spallation resistance ($x \leq 25$ at.%) or led to complete disintegration ($x > 25$ at.%). Among the (NbMo)-containing alloys, the $(HfCo)_{90}(NbMo)_{10}$ alloy with the dual-phase bcc+B2 structure showed the most promising oxidation resistance. This alloy withstood cyclic oxidation up to 15 h with a mass gain close to the HfCo alloy and survived 100 h without changes in geometry of the specimen. Unlike the HfCo alloy, in the $(HfCo)_{90}(NbMo)_{10}$ alloy, the external CoO layer was found already after 1 h. The effect of chemical and phase compositions on the formation of certain oxides was discussed. Comparison with the other refractory high-entropy alloys was also presented.

Keywords: refractory high-entropy alloys; oxidation behaviour; bcc+B2 structure; spallation resistance

check for updates

Citation: Yurchenko, N.; Panina, E.; Zherebtsov, S.; Stepanov, N. Oxidation Behaviour of Refractory $(HfCo)_{100-x}(NbMo)_x$ High-Entropy Alloys with a bcc+B2 Structure. *Appl. Sci.* **2023**, *13*, 9336. https://doi.org/10.3390/app13169336

Academic Editor: Eiji Tokunaga

Received: 26 July 2023
Revised: 16 August 2023
Accepted: 16 August 2023
Published: 17 August 2023

Copyright: © 2023 by the authors. Licensee MDPI, Basel, Switzerland. This article is an open access article distributed under the terms and conditions of the Creative Commons Attribution (CC BY) license (https://creativecommons.org/licenses/by/4.0/).

1. Introduction

For nearly 80 years, nickel-based superalloys have served as the preferred materials for the hottest parts of gas turbines. However, an ongoing need to increase the performance of these systems requires materials that can operate at higher temperatures. Among the potential candidates, refractory high-entropy alloys (RHEAs) are considered the most promising, because of their excellent strength at ultra-high temperatures and phase stability [1–4].

However, for high-temperature service, oxidation resistance is essential. It is known that most refractory metals and alloys are vulnerable to oxidation at T > 500 °C due to the formation of volatile oxides (e.g., MoO_3, WO_3, V_2O_5). While the oxidation resistance of some RHEAs is similarly inferior [5–10], certain RHEAs can withstand oxygen attack up to 1500 °C thanks to complex oxides [11–13]. For instance, Al-Cr-Nb-Mo-Ta-Ti system RHEAs tend to the form a protective rutile-type $CrTaO_4$ oxide stemming from a reaction between Cr_2O_3 and Ta_2O_5 oxides [12,14–16]. Unlike traditional Al_2O_3 and Cr_2O_3 oxides that appear as dense external layers, $CrTaO_4$ nucleates beneath a mixture ($Al_2O_3 + Cr_2O_3 + TiO_2$) of discontinuous scales and does not prevent internal oxidation, yet effectively blocks the outward diffusion of metal cations [15]. Another rutile-type $CrNbO_4$ oxide has been found to be responsible for good oxidation resistance of Al-Cr-Nb-Ti-Zr system RHEAs [17–21]. Occasionally, Cr alloying is more attractive for improvement of the oxidation resistance of RHEAs compared to Al additions [22]. However, in some Cr-free RHEAs, a fair protectiveness is provided by $AlNbO_4$, Ti_2ZrO_6, $Ti_7Al_2O_{15}$, and $Ta_2Nb_4O_{15}$ oxides [23,24].

Unfortunately, most studies of the oxidation behaviour of RHEAs are performed in isothermal conditions [11,13,17,18,20,21,23–29]. This testing scheme is suitable for establishing the oxidation kinetics and oxidation mechanisms, but it does not allow for estimating the response of the alloy to repeated heating–cooling cycles that usually occur during service life. Cyclic testing can induce the spallation of oxide scale and even disintegration of the specimen due to the accumulation of thermal stresses [30]. A recent report [31] revealed the trade-off between the oxidation and spallation/disintegration resistances in RHEAs, which was highly dependent on the chemical and phase compositions. Specifically, an increase in Al concentration deteriorated the spallation/disintegration resistance due to a large volume fraction of brittle Laves phase despite lower mass gains at early stages of oxidation compared to alloys with reduced Al content.

Existing studies focus on RHEAs consisting exclusively of refractory metals with additions of Al, Cr, or Si [15]. In contrast, the recently introduced RHEAs, containing late transition metals, open new directions for designing high-performance alloys [32–39]. One of the examples is a series of $(HfCo)_{100-x}(NbMo)_x$ alloys that have demonstrated good room-temperature plasticity while retaining high strength at 1000 °C [34,36]. Such a combination of properties was achieved in dual-phase alloys comprised of a "soft" (Hf, Co)-rich B2 matrix (hardness of 6.5–8.4 GPa) with embedded "hard" (Nb, Mo)-rich particles (hardness of 7.5–9.3 GPa). This bcc+B2 structure was stable after 700 h of annealing at 1000 °C [40], thereby outperforming the temperature limit for microstructural degradation of many RHEAs [41–45]. However, the oxidation behaviour of RHEAs containing late transition metals is yet to be investigated. In the current work, which, to the best authors' knowledge, was the first report of its type, we performed a comprehensive analysis of the oxidation kinetics and mechanisms, as well as the spallation/disintegration resistance, of the $(HfCo)_{100-x}(NbMo)_x$ RHEAs subjected to cyclic oxidation at 1000 °C. Data obtained in this study appear to be novel both in terms of understanding the role of chemical and phase compositions on the oxidation behaviour of RHEAs containing late transition metals, and, more broadly, in terms of evaluating the potential of these alloys as high-temperature materials under conditions close to service ones.

2. Materials and Methods

Vacuum arc melting (Arc Melter AM 200 (Edmund Bühler GmbH, Bodelshausen, Germany)) of pure ($\geq$ 99.9 wt. %) metals was used to produce laboratory-scale (20 g) ingots of the alloys with the nominal compositions of HfCo, $(HfCo)_{90}(NbMo)_{10}$, $(HfCo)_{75}(NbMo)_{25}$, $(HfCo)_{40}(NbMo)_{60}$, $(HfCo)_{25}(NbMo)_{75}$, and NbMo (at. %). From the as-cast ingots, the rectangular ($6 \times 4 \times 4$ mm^3) samples were cut by electric discharge machine. The specimens were mechanically gritted and polished, then ultrasonically cleaned in isopropanol.

A Nabertherm furnace (LT 5/12/P320, Nabertherm, Lilienthal/Bremen, Germany) was used for oxidation tests under static laboratory air at 1000 °C for 100 h. The samples were put on alumina plates, then placed into the preheated furnace and held there for 1 h, 5 h, and further with intervals of every 5 h. After each period of oxidation test, the samples were cooled in the laboratory air for mass measurements. This process was repeated until reaching 100 h or complete disintegration of the specimen, whichever occurred first. Mass measurements were performed using an HR-200 analytical balance (A&D Company, Ltd., Tokyo, Japan) with an accuracy of 0.1 mg. Only bulk samples were weighed after oxidation. The spalled oxide scales or fragmented parts of the specimens were not included. At least two specimens were tested for each alloy.

X-ray diffraction (XRD) was employed for phase identification of the oxides in the scales using a Rigaku diffractometer (Rigaku Corporation, Tokyo, Japan) with Cu-Kα radiation; the scanning rate was 4°/min and the 2Θ was in a range of 20–100°. Cross-sections of the oxidized specimens were studied using an FEI Quanta 600 FEG (Thermo Fisher Scientific, Brno, Czech Republic) scanning electron microscope (SEM) with back-scattered electron (BSE) and energy-dispersive X-ray spectroscopy (EDS) detectors. Samples for SEM studies were mounted in Buehler KonductoMet via Buehler SimpliMet

4000 mounting press (Buehler, Lake Bluff, IL, USA) to preserve the integrity of the oxide scale. The mounted specimens were polished using a Buehler VibroMet 2 Vibratory Polisher (Buehler, Lake Bluff, IL, USA) and Buehler MasterMet 2 Suspension to mirror surfaces.

3. Results

3.1. Initial Structure

The initial microstructure of the $(HfCo)_{100-x}(NbMo)_x$ alloys has been reported in detail elsewhere [34,36,40]. Figure 1 gives a brief description of non-oxidized microstructures to provide context for further discussions. The HfCo alloy (Figure 1a) had a nearly single-phase microstructure composed of large B2 grains, the boundaries of which were decorated with sporadic (the volume fraction was less than 1%) nanometre-sized HfO_2 particles (white entities in Figure 1a). Additions of $(NbMo)_x$ in the concentration interval of $10 \leq x \leq 75$ at.% (Figure 1b–e) initiated the formation of (Nb, Mo)-rich bcc particles (dark Z-contrast) embedded in a (Hf, Co)-rich B2 matrix (bright Z-contrast). The volume fraction of the bcc phase, f_{bcc}, varied from ~13% in the $(HfCo)_{90}(NbMo)_{10}$ alloy to ~76% in the $(HfCo)_{25}(NbMo)_{75}$ alloy. The NbMo alloy (Figure 1f) showed an almost single-phase microstructure presented by bcc grains and traces (<1%) of the tiny HfO_2 particles (white entities in Figure 1f).

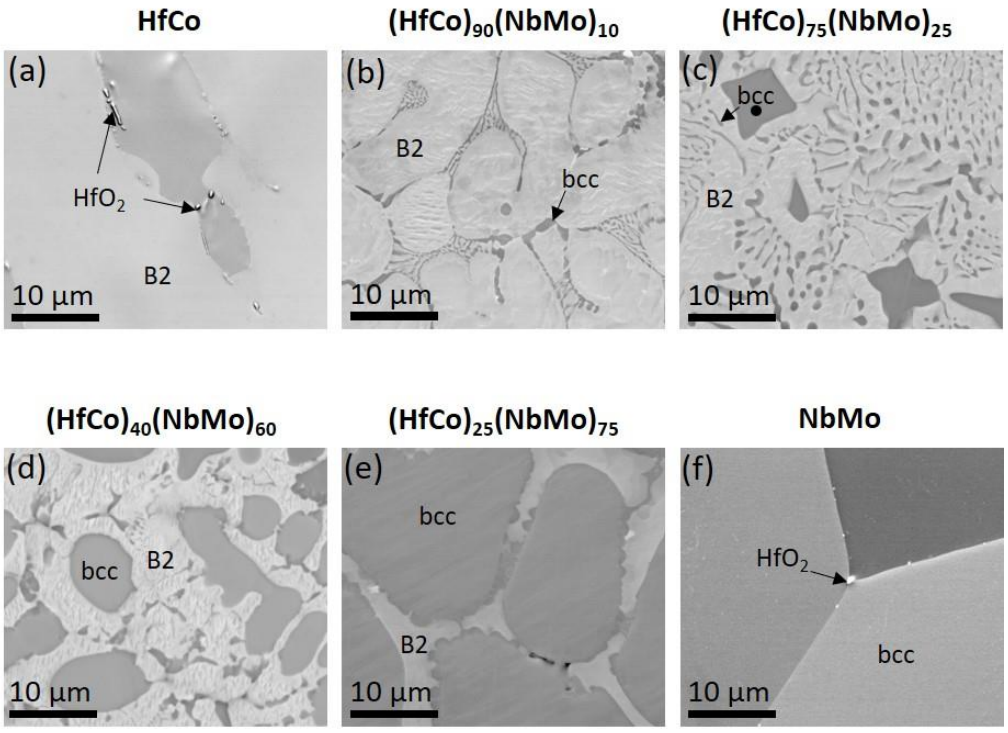

Figure 1. SEM-BSE images of the initial microstructure of the $(HfCo)_{100-x}(NbMo)_x$ alloys: (**a**) HfCo; (**b**) $(HfCo)_{90}(NbMo)_{10}$; (**c**) $(HfCo)_{75}(NbMo)_{25}$; (**d**) $(HfCo)_{40}(NbMo)_{60}$; (**e**) $(HfCo)_{25}(NbMo)_{75}$; (**f**) NbMo.

3.2. Oxidation Behaviour

Figure 2 plots the mass gain data obtained at 1000 °C and overall appearance of the specimens after the tests. The single-phase B2-ordered HfCo alloy showed a continuous mass gain, achieving 74.2 mg/cm^2 after 100 h (Figure 2a). The mass gain of the dual-phase bcc+B2 $(HfCo)_{90}(NbMo)_{10}$ alloy with f_{bcc} = 13% was close to that of the HfCo alloy until 15 h, followed by a nearly constant value of ~30 mg/cm^2. Some variations in mass gain at this stage could be an indication of the oxide scale spallation. In the dual-phase bcc+B2 $(HfCo)_{75}(NbMo)_{25}$ alloy with f_{bcc} = 28%, the spallation commenced already after 1 h, judging from the mass gain vs. time dependence. Only these three alloys survived

after 100 h, and only the HfCo alloy retained a pristine form (Figure 2b). The specimen of the $(HfCo)_{90}(NbMo)_{10}$ alloy was partially spalled off, yet it saved its geometry and some regions with an intact oxide scale. The $(HfCo)_{75}(NbMo)_{25}$ alloy experienced a more serious oxidation resulting in loss of integrity along the edge surfaces and some bending of the oxidized remnants (Figure 2b).

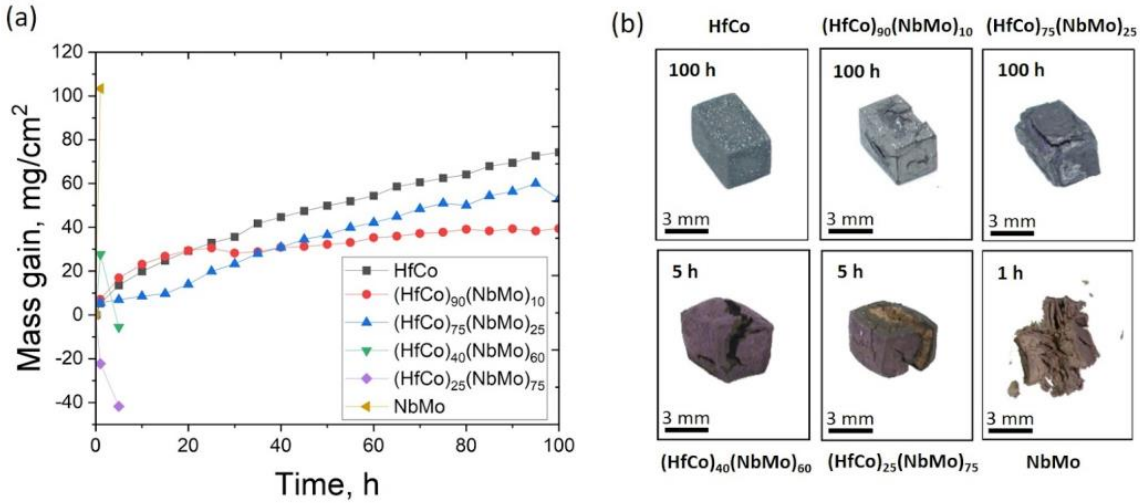

Figure 2. Mass gains for the $(HfCo)_{100-x}(NbMo)_x$ alloys after cyclic oxidation tests at 1000 °C (**a**); an overall view of the oxidized alloys after certain periods (**b**).

The other three alloys, namely, dual-phase bcc+B2 $(HfCo)_{40}(NbMo)_{60}$ (f_{bcc} = 51%) and $(HfCo)_{25}(NbMo)_{75}$ (f_{bcc} = 76%) and single-phase bcc NbMo, demonstrated either rapid mass gain or mass loss (Figure 2a). Visual inspection revealed complete disintegration of the specimens of the $(HfCo)_{40}(NbMo)_{60}$ and $(HfCo)_{25}(NbMo)_{75}$ alloys after 5 h, while the NbMo alloy oxidized already after 1 h (Figure 2b).

For the HfCo and $(HfCo)_{90}(NbMo)_{10}$ alloys, we evaluated the oxidation kinetics according to a well-known equation [46]:

$$\Delta m = kt^n, \quad (1)$$

where Δm—the mass gain per unit surface area (mg/cm^2); k—the oxidation rate constant (mg/cm^2 h); t—time (h); and n—the time exponent. The entire curve of the HfCo alloy can be fitted using n = 0.58 and k = 5.23 mg/cm^2 h$^{0.58}$, indicating near-parabolic oxidation kinetics. In a part of the curve (0–15 h) prior to the spallation, the $(HfCo)_{90}(NbMo)_{10}$ alloy also displayed a near-parabolic regime with n = 0.46 and k = 7.75 mg/cm^2 h$^{0.46}$.

3.3. Structure after Oxidation

To better understand the underlying processes occurred during the oxidation, we investigated the cross-sections and surfaces of the specimens in the beginning (1 h) and end (100 h) of the tests. Only the survived HfCo, $(HfCo)_{90}(NbMo)_{10}$, and the $(HfCo)_{75}(NbMo)_{25}$ alloys were taken for detailed studies.

3.3.1. Cross-Section Analysis after 1 h

Figure 3 illustrates the cross-sections of the HfCo, $(HfCo)_{90}(NbMo)_{10}$, and $(HfCo)_{75}(NbMo)_{25}$ alloys after 1 h of oxidation. In the HfCo alloy (Figure 3a), the top of the oxidized specimen was covered by a ~10 μm-thick oxide layer (OL). The OL was enriched with Hf and appeared to be rather dense (Figure 3a, Table 1). Beneath the OL, a ~20 μm-thick internally reacted zone (IRZ) was located. Inside the IRZ, we found alternate (Hf, O)-rich and Co-rich (O-lean) areas. The bottom part of the IRZ was decorated with a ~4 μm-thick dense Co-rich layer (Figure 3a, Table 1).

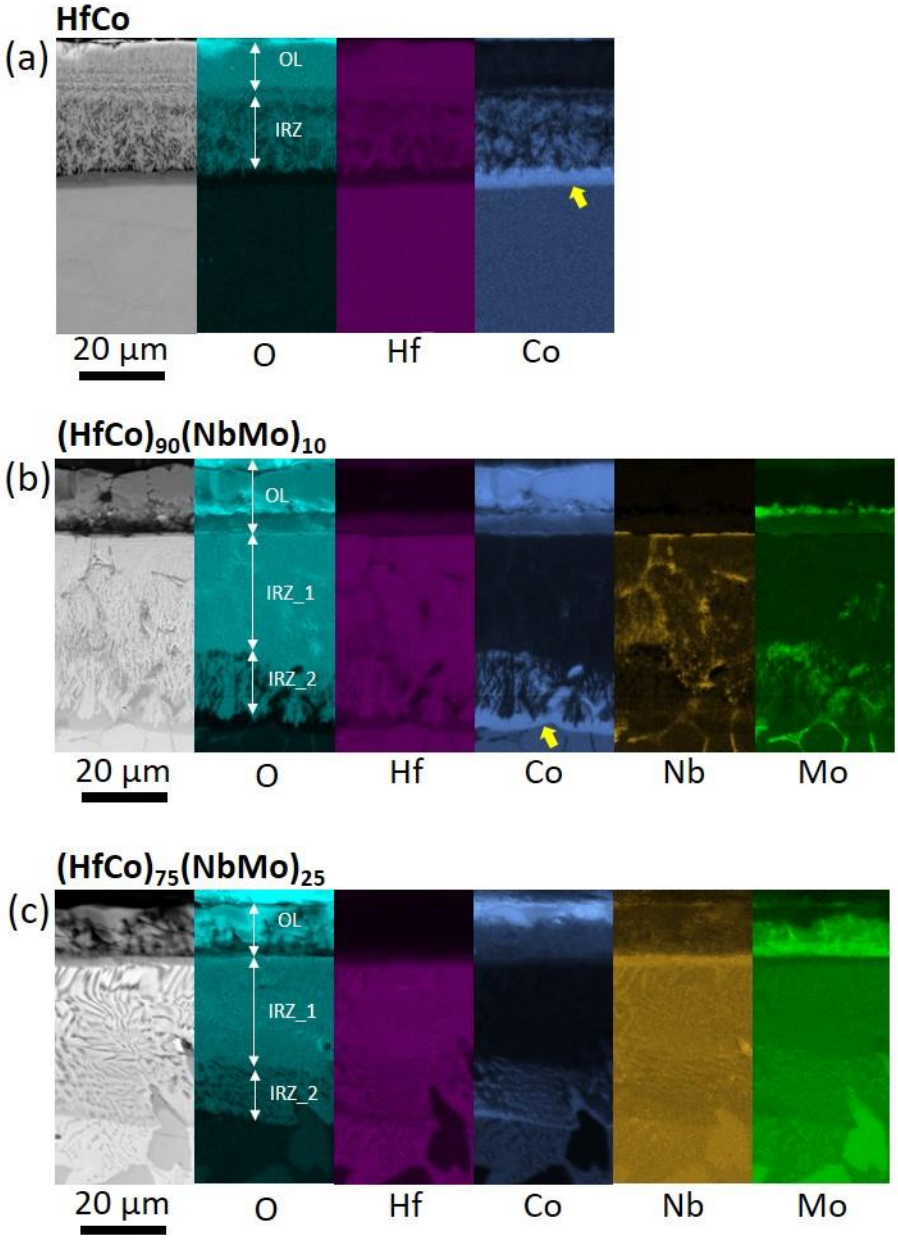

Figure 3. Characterisation of typical cross-section areas of the HfCo (**a**), $(HfCo)_{90}(NbMo)_{10}$ (**b**), and $(HfCo)_{75}(NbMo)_{25}$ (**c**) alloys oxidized at 1000 °C for 1 h: SEM-BSE images combined with SEM-EDS maps. On the maps of the O distribution, the oxide layer (OL) and the internal reaction zone (IRZ) are denoted. In the $(HfCo)_{90}(NbMo)_{10}$ (**b**) and $(HfCo)_{75}(NbMo)_{25}$ (**c**) alloys, the IRZ consisted of IRZ_1 and IRZ_2 with higher and lower concentration of O, respectively. Yellow arrows in the Co distribution maps of the HfCo (**a**) and $(HfCo)_{90}(NbMo)_{10}$ (**b**) alloys highlight the formation of a Co-rich layer on the boundary between the IRZ and an unoxidized core.

Unlike the HfCo alloy, a ~10 µm-thick OL of the $(HfCo)_{90}(NbMo)_{10}$ alloy was enriched with Co (Figure 3b, Table 1). The OL was dense, though it contained occasional cracks and pores. The bottom part of the OL was framed with a thin and discontinuous Mo-rich layer. Below the OL, a ~45 µm-thick IRZ composed of two characteristic regions was located (Figure 3b, Table 1). The top of the first ~30 µm-thick region in the IRZ (IRZ_1) was covered by thin (Nb, Co)-rich islands. The remaining part of IRZ_1 was presented by a mixture of internally reacted B2 grains and bcc interlayers. Notably, the former B2 grains were mostly composed of Hf, while the bcc interlayers were enriched with Nb. The Co content was reduced in this region; Mo appeared to be evenly distributed. As the O penetration

deepened, IRZ_1 transitioned to IRZ_2, the overall constitution of which partly resembled that of the IRZ found in the HfCo alloy. Specifically, there were Co-rich (and O-lean) zones that filled the gaps between Hf-rich areas. The distribution of Mo in this zone was similar to Co. Analogous to the HfCo alloy, the boundary between the IRZ and unoxidized core was delineated by a ~3 μm-thick Co-rich layer (Figure 3b, Table 1).

Table 1. Average chemical compositions of the characteristic layers formed in the cross-sections of the HfCo, $(HfCo)_{90}(NbMo)_{10}$, and $(HfCo)_{75}(NbMo)_{25}$ alloys oxidized at 1000 °C for 1 h.

Area of EDS Analysis	Elements, at. %				
	Hf	Co	Nb	Mo	O
			HfCo		
OL	48.9	10.0	-	-	41.1
IRZ	42.8	36.0	-	-	21.2
Co-rich layer	21.7	78.3	-	-	-
			$(HfCo)_{90}(NbMo)_{10}$		
OL	2.1	41.0	0.1	0.2	57.6
IRZ_1	21.5	4.4	2.7	1.0	70.4
IRZ_2	21.1	22.5	1.2	3.1	52.1
Co-rich layer	21.3	61.7	1.2	1.9	13.9
			$(HfCo)_{75}(NbMo)_{25}$		
OL	0.8	35.6	1.9	10.9	50.9
IRZ_1	42.8	5.2	5.4	0.2	46.4
IRZ_2	32.1	36.8	4.0	4.5	22.7

Compared to the HfCo and $(HfCo)_{90}(NbMo)_{10}$ alloys, the ~10 μm-thick OL of the $(HfCo)_{75}(NbMo)_{25}$ alloy was rather loose (Figure 3c). Its upper part was covered by a Co-rich layer, while the bottom part was enriched with Mo (Figure 3c, Table 1). A ~35 μm-thick IRZ, the outmost part of which was wetted with a (Nb, Co)-rich layer, was found beneath. Similar to the $(HfCo)_{90}(NbMo)_{10}$ alloy, the IRZ was composed of two specific regions, namely IRZ_1 and IRZ_2. The microstructure of both regions replicated that of unoxidized core, yet differed in the distribution of constitutive elements. Specifically, inside IRZ_1, we found former B2 and bcc lamellae, which were composed of Hf and Nb, respectively. Meanwhile, this region was lean in Co and Mo. Within IRZ_2, profuse Co-rich (and O-lean) islands surrounded by Hf-rich lamellae were found. A tiny discontinuous Co-rich layer that separated the bottom part of IRZ_2 and unoxidized core should also be noted (Figure 3c, Table 1).

3.3.2. Cross-Section Analysis after 100 h

After 100 h, remarkable changes in the constitution of the cross-sections were revealed. The OL of the HfCo alloy became Co-rich, thicker (~70 μm), and contained some porosity (Figure 4a, Table 2). The IRZ deepened (with a total thickness of ~750 μm) and developed into two zones with no clear difference in chemical composition between them. The only difference was the O content: the much-thicker IRZ_1 was richer in O compared to IRZ_2. In the bottom part of IRZ_1 and inside IRZ_2, we found thin lateral cracks, the surfaces of which were covered with Co-rich layers. Similar to 1 h-oxidation, the interface between the IRZ and the unoxidized core was decorated with the dense Co-rich layer (Figure 4a, Table 2).

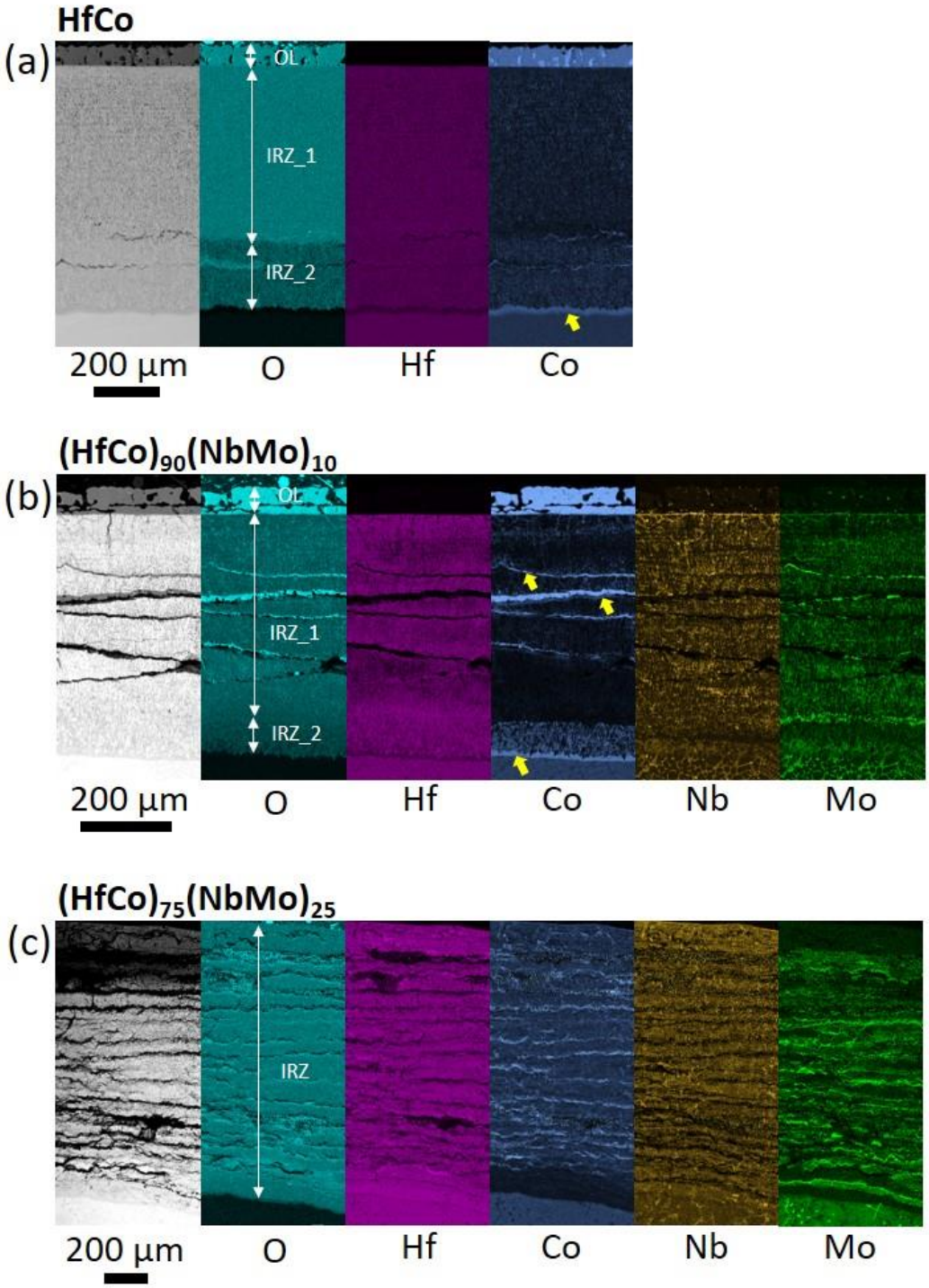

Figure 4. Characterisation of typical cross-section areas of the HfCo (**a**), $(HfCo)_{90}(NbMo)_{10}$ (**b**), and $(HfCo)_{75}(NbMo)_{25}$ (**c**) alloys oxidized at 1000 °C for 100 h: SEM-BSE images combined with SEM-EDS maps. On the maps of the O distribution, the OL and IRZ are denoted. In the $(HfCo)_{75}(NbMo)_{25}$ (**c**) alloy, only IRZ is presented. Yellow arrows in the Co distribution maps of the HfCo (**a**) and $(HfCo)_{90}(NbMo)_{10}$ (**b**) alloys highlight the formation of Co-rich layers, which covered surfaces of cracks inside the IRZ and the boundary between the IRZ and the unoxidized core.

In the $(HfCo)_{90}(NbMo)_{10}$ alloy, we examined the areas of the cross-sections that remained intact (see Figure 2b). We found that the OL in these areas remained Co-rich, while becoming looser (Figure 4b, Table 2). Inheriting a two-region constitution, the IRZ of the $(HfCo)_{90}(NbMo)_{10}$ alloy was thinner (~530 µm) compared to that of the HfCo alloy.

However, we found numerous large lateral cracks in the central part of IRZ_1. The upper surfaces of these cracks were covered with continuous Co-rich layers and discontinuous Mo-rich islands. In turn, the specific elemental distribution inside IRZ_2 resembled that of 1 h-oxidation, with a clear separation between Hf-rich and Co-rich (and O-lean) regions. Beneath, there was also the Co-rich layer that delineated the IRZ from the unoxidized core (Figure 4b, Table 2).

Table 2. Average chemical compositions of the characteristic layers formed in the cross-sections of the HfCo, $(HfCo)_{90}(NbMo)_{10}$, and $(HfCo)_{75}(NbMo)_{25}$ alloys oxidized at 1000 °C for 100 h.

Area of EDS Analysis	Elements, at. %				
	Hf	Co	Nb	Mo	O
			HfCo		
OL	0.8	40.1	-	-	59.1
IRZ_1	18.2	13.8	-	-	68.0
IRZ_2	21.7	22.0	-	-	56.3
Co-rich layer	16.3	71.9	-	-	11.8
			$(HfCo)_{90}(NbMo)_{10}$		
OL	0.3	42.4	0.7	0.4	56.2
IRZ_1	14.5	6.8	2.4	1.2	75.2
IRZ_2	20.0	21.0	0.9	2.2	55.9
Co-rich layer	10.9	66.1	2.4	2.8	17.8
			$(HfCo)_{75}(NbMo)_{25}$		
Top of the IRZ	13.6	12.6	5.4	0.9	68.6
Middle of the IRZ	10.2	12.7	4.2	3.3	69.6
Bottom of the IRZ	12.6	2.8	3.5	4.4	76.7

Since the $(HfCo)_{75}(NbMo)_{25}$ alloy experienced multiple spallation events, no external OL was found and only a part of IRZ could be identified (Figure 4c). The ~1300 µm IRZ was composed of numerous alternate layers separated by large cracks, the surfaces of which were framed with thick Mo-rich layers and thin Co-rich islands (Figure 4b, Table 2). Notably, the top of the IRZ was depleted of Mo, while its bottom part was lean in Co, in contrast to the HfCo and $(HfCo)_{90}(NbMo)_{10}$ alloys.

3.3.3. Surface Analysis

The oxides on the surface of the HfCo, $(HfCo)_{90}(NbMo)_{10}$, and $(HfCo)_{75}(NbMo)_{25}$ alloys were identified by XRD analysis. After 1 h of oxidation (Figure 5a), the surface of the HfCo alloy was covered by two different types of a HfO_2 oxide, denoted as HfO_2_14 (ZrO_2-b-prototype; mP12) [47] and HfO_2_225 (CaF_2-prototype; cF12) [48]. The most intensive Bragg's peaks belonged to HfO_2_225, while HfO_2_14 presented a series of low-intensity reflections.

In the $(HfCo)_{90}(NbMo)_{10}$ and $(HfCo)_{75}(NbMo)_{25}$ alloys, four different oxides were found, namely CoO (NaCl-prototype; cF8) [49], HfO_2_14, $Nb_2Co_4O_9$ ($Nb_2Mn_4O_9$-prototype; hP30) [50], and MoO_3 (MoO_3-prototype; oP16) [51] (Figure 5a). CoO dominated in both alloys, while, the intensity and number of the Bragg's peaks corresponding to other three oxides in the $(HfCo)_{75}(NbMo)_{25}$ alloy were notably higher compared to the $(HfCo)_{90}(NbMo)_{10}$ alloy.

After 100 h of oxidation (Figure 5b), CoO became the dominant oxide in the HfCo alloy; traces of HfO_2_14 were also detected. While CoO still prevailed in the $(HfCo)_{90}(NbMo)_{10}$ alloy and no new oxides were identified, we observed the increased intensity of HfO_2_14 and $Nb_2Co_4O_9$ and the appearance of several new low-intensity reflections belonging to MoO_3. In the $(HfCo)_{75}(NbMo)_{25}$ alloy, we revealed the dominance of $Nb_2Co_4O_9$, HfO_2_14, and MoO_3. The intensity of the diffraction maximums related to CoO were significantly lower compared to those of 1h-oxidation (Figure 5b).

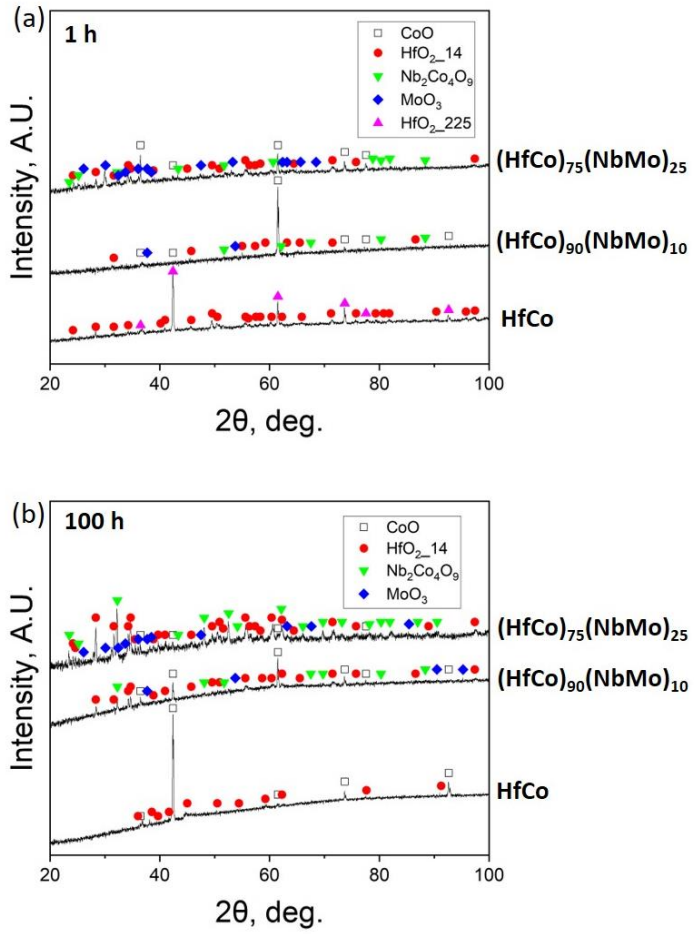

Figure 5. XRD patterns collected from the surfaces of the HfCo, $(HfCo)_{90}(NbMo)_{10}$, and $(HfCo)_{75}(NbMo)_{25}$ alloys oxidized at 1000 °C for 1 (**a**) and 100 (**b**) h.

4. Discussion

4.1. Oxidation Behaviour

The results of this study show that the chemical and phase composition has a profound effect on the oxidation behaviour of the $(HfCo)_{100-x}(NbMo)_x$ alloys during cyclic testing at 1000 °C. The single-phase B2-ordered HfCo alloy demonstrated the best oxidation and spallation/disintegration resistances. Dual-phase bcc+B2 $(HfCo)_{90}(NbMo)_{10}$ and $(HfCo)_{75}(NbMo)_{25}$ alloys with $f_{bcc} \leq 30\%$ could withstand spallation at short exposures and preserved an acceptable level of the integrity after 100 h, but, when $f_{bcc} > 50\%$ in the $(HfCo)_{40}(NbMo)_{60}$ and $(HfCo)_{25}(NbMo)_{75}$ alloys, the alloys disintegrated rapidly. The single-phase bcc NbMo alloy appeared to be the most vulnerable to oxygen attack and disintegrated completely after 1 h.

Analysis of oxidation kinetics (Equation (1)), which could only be performed for the HfCo and $(HfCo)_{90}(NbMo)_{10}$ alloys, revealed a near-parabolic regime in both alloys that was an indication of a diffusion-controlled oxidation mechanism, involving the formation of the protective scales. In the HfCo alloy, the protection was provided by the external HfO_2 or CoO scales formed at early (1 h) or late (100 h) stages, respectively (Figures 3a, 4a, and 5; Tables 1 and 2). In turn, the addition of $(NbMo)_x$ could alleviate the outward diffusion of Co, leading to the creation of the CoO layer on the top surface of the oxidized $(HfCo)_{90}(NbMo)_{10}$ alloy from the initial stages of oxidation (Figures 3b, 4b, and 5; Tables 1 and 2). In the latter alloy, CoO could also be considered as the protective oxide, which seemed to partially counter the negative effect of the presence of the (Nb, Mo)-rich bcc phase. Specifically, CoO could (i) block the outward diffusion of Mo and (ii) prevent

the possible emergence of binary Nb-rich oxides [8] due to scavenging of the Nb cations to a complex $Nb_2Co_4O_9$ oxide(Figure 5).

In the meantime, the external CoO layer was permeable for the inward diffusion of O that resulted in the development of deep internally reacted zones in the HfCo and $(HfCo)_{90}(NbMo)_{10}$ alloys as the testing time progressed. These IRZs consisted of a dominant HfO_2 and, in the case of the $(HfCo)_{90}(NbMo)_{10}$ alloy, traces of $Nb_2Co_4O_9$ and MoO_3 (Figures 3a,b and 4a,b; Tables 1 and 2). Although no spallation occurred in the HfCo alloy, we observed occasional cracks originated, most likely, from the repeated heating–cooling cycles [52–54]. In the $(HfCo)_{90}(NbMo)_{10}$ alloy, the cracks could additionally appear due to the nucleation of the fast-growing and highly volatile MoO_3 [14]. However, although the single-phase B2-ordered HfCo alloy was extremely ductile [36] and capable of preventing the propagation of the cracks and, thus, to avoid the spallation, the less ductile dual-phase bcc+B2 $(HfCo)_{90}(NbMo)_{10}$ alloy remained pristine for a much shorter period of time, accumulating the stresses which were finally relieved by partial spallation [31].

The poor oxidation and spallation/disintegration resistances of other alloys could be rationalized by the example of the $(HfCo)_{75}(NbMo)_{25}$ alloy (Figures 3c and 4c). Despite the CoO layer that also covered the 1 h-oxidized $(HfCo)_{75}(NbMo)_{25}$ alloy, it was unable to protect this alloy due to its loose constitution. Simultaneously, the high fraction of the (Nb, Mo)-rich bcc phase that served as reservoirs for the harmful MoO_3 intensified the spallation (Figure 4c). Eventually, the further (in dual-phase alloys) or complete (in the NbMo alloy) replacement of the B2 phase, standing as a provider for CoO, with the bcc phase aggravated the oxidation resistance and ability to sustain spallation/disintegration to an unacceptable level, making the potential application of these alloys impossible without protective coatings [55].

4.2. Comparison with Other RHEAs

To understand the protection level, which was provided by CoO, we compared the mass gain values obtained after 1 h of oxidation at 1000 °C for the $(HfCo)_{90}(NbMo)_{10}$ alloy and other RHEAs [9,18,19,21,23,24,31,56–60] (Figure 6). This period of time was chosen to minimize the evaporation effects that accounted for misleading values of the mass gain and to cover a higher number of the alloys available in the literature. We found that the CoO-forming $(HfCo)_{90}(NbMo)_{10}$ alloy showing 7.1 mg/cm^2 could not compete with RHEAs, the oxidation resistance of which relied on the rutile-type $CrTaO_4$, gaining only 0.2 mg/cm^2 [56]. Meantime, the $(HfCo)_{90}(NbMo)_{10}$ alloy appeared to be more oxidation-resistant compared to RHEAs protected by another rutile-type $CrNbO_4$ [17] or $AlTaO_4$ [59] scales, or by layers composed of discontinuous complex ($AlNbO_4$, Ti_2ZrO_6) and simple (Al_2O_3, Cr_2O_3, ZrO_2, TiO_2) oxides [23,60] (Figure 6).

The $(HfCo)_{90}(NbMo)_{10}$ alloy also showed a better oxidation resistance compared to a commercial Nb alloy C103 [1], which is used only in a coated state in aerospace propulsion systems as thrust cones and high-temperature valves or in turbine engines as thrust augmenter flaps. Bearing in mind the promising mechanical properties [36], which can be improved by a proper heat treatment [40], excellent phase stability [40], and acceptable oxidation/spallation resistance in an uncoated state that provides some protectiveness in the case of coating failure, the $(HfCo)_{90}(NbMo)_{10}$ alloy examined in the present work appears to be a potential candidate for high-temperature applications, for instance, as turbine blades, nozzles, and/or thrust augmenter flaps.

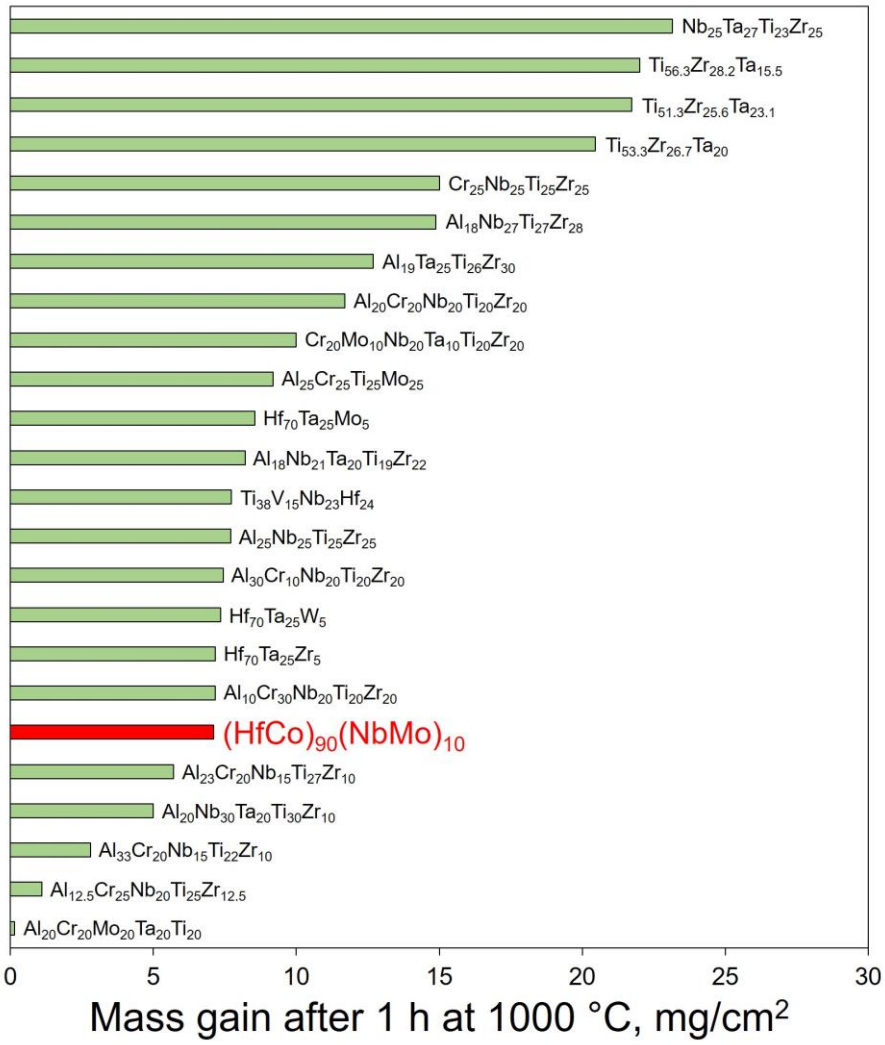

Figure 6. Comparison of the mass gain after 1 h at 1000 °C of the $(HfCo)_{90}(NbMo)_{10}$ alloy and other RHEAs [9,18,19,21,23,24,31,56–60].

5. Conclusions

In this study, the oxidation behaviour of the bcc+B2 $(HfCo)_{100-x}(NbMo)_x$ (x = 0; 10; 25; 40; 75; 100 (at.%)) RHEAs during cyclic oxidation at 1000 °C was investigated. The following conclusions were drawn:

(1) The single-phase B2-ordered HfCo alloy demonstrated the best spallation resistance and retained a pristine form after 100 h. The near-parabolic oxidation kinetics of the HfCo alloy with n = 0.58 and k = 5.23 mg/cm^2 h$^{0.58}$ was found. The protection was provided by the formation of the external HfO_2 or CoO layers after 1 or 100 h, respectively.

(2) In the (NbMo)-containing alloys, the oxidation and spallation/disintegration resistances degraded with an increase in the fraction of the (Nb, Mo)-rich bcc phase that acted as a reservoir for the harmful MoO_3. Only the $(HfCo)_{90}(NbMo)_{10}$ alloy with ~13% of the bcc phase could withstand the spallation up to 15 h and preserved the acceptable integrity after 100 h, while the alloys with >50% of the bcc phase oxidized and disintegrated completely after 1–5 h.

(3) Before spallation, the $(HfCo)_{90}(NbMo)_{10}$ alloy showed near-parabolic oxidation kinetics with n = 0.46 and k = 7.75 mg/cm^2 h$^{0.46}$. Unlike the HfCo alloy, the protection of the $(HfCo)_{90}(NbMo)_{10}$ alloy initially relied on the exclusive CoO layer. Due to this, the $(HfCo)_{90}(NbMo)_{10}$ alloy was more oxidation-resistant compared to many other RHEAs covered by scales composed of complex and/or simple oxides.

Author Contributions: Conceptualization, N.Y., E.P. and N.S.; methodology, N.Y. and E.P.; validation, N.Y., E.P. and N.S.; formal analysis, N.Y. and E.P.; investigation, E.P.; data curation, N.Y., S.Z. and N.S.; writing—original draft preparation, N.Y.; writing—review and editing, N.Y., E.P., S.Z. and N.S.; visualization, N.Y. and E.P.; supervision, N.Y., S.Z. and N.S. All authors have read and agreed to the published version of the manuscript.

Funding: This work was supported by the Russian Science Foundation, Grant no. 19-79-30066 (https://rscf.ru/en/project/19-79-30066/ (accessed on 26 July 2023)). A part of this research (XRD characterisation) was partially funded by the Ministry of Science and Higher Education of the Russian Federation as part of the World-Class Research Center program: Advanced Digital Technologies (Contract no. 075-15-2022-312 dated 20 April 2022).

Institutional Review Board Statement: Not applicable.

Informed Consent Statement: Not applicable.

Data Availability Statement: The data presented in this study are available on request from the corresponding author.

Acknowledgments: The work was carried out using the equipment of the Joint Research Center of Belgorod State National Research University «Technology and Materials». The authors also thank S. Naumov, Belgorod National Research University, for aid in preparing the ingots of the alloys.

Conflicts of Interest: The authors declare no conflict of interest.

References

1. Senkov, O.N.; Miracle, D.B.; Chaput, K.J.; Couzinie, J.P. Development and Exploration of Refractory High Entropy Alloys—A Review. *J. Mater. Res.* **2018**, *33*, 3092–3128. [CrossRef]
2. Wei, Q.; Xu, X.; Shen, Q.; Luo, G.; Zhang, J.; Li, J.; Fang, Q.; Liu, C.-T.; Chen, M.; Nieh, T.-G.; et al. Metal-Carbide Eutectics with Multiprincipal Elements Make Superrefractory Alloys. *Sci. Adv.* **2022**, *8*, eabo2068. [CrossRef] [PubMed]
3. Zhang, Y.; Wei, Q.; Xie, P.; Xu, X. An Ultrastrong Niobium Alloy Enabled by Refractory Carbide and Eutectic Structure. *Mater. Res. Lett.* **2022**, *11*, 169–178. [CrossRef]
4. Sun, B.; Mo, J.; Wang, Q.; Chen, Y.; Zhang, Z.; Shen, B.; Liang, X. Outstanding Specific Yield Strength of a Refractory High-Entropy Composite at an Ultrahigh Temperature of 2273 K. *J. Mater. Sci. Technol.* **2023**, *166*, 145–154. [CrossRef]
5. Liu, C.M.; Wang, H.M.; Zhang, S.Q.; Tang, H.B.; Zhang, A.L. Microstructure and Oxidation Behavior of New Refractory High Entropy Alloys. *J. Alloys Compd.* **2014**, *583*, 162–169. [CrossRef]
6. Chang, C.; Titus, M.S.; Yeh, J. Oxidation Behavior between 700 and 1300 °C of Refractory TiZrNbHfTa High-Entropy Alloys Containing Aluminum. *Adv. Eng. Mater.* **2018**, *20*, 1700948. [CrossRef]
7. Sheikh, S.; Bijaksana, M.K.; Motallebzadeh, A.; Shafeie, S.; Lozinko, A.; Gan, L.; Tsao, T.-K.; Klement, U.; Canadinc, D.; Murakami, H.; et al. Accelerated Oxidation in Ductile Refractory High-Entropy Alloys. *Intermetallics* **2018**, *97*, 58–66. [CrossRef]
8. Yurchenko, N.; Panina, E.; Zherebtsov, S.; Salishchev, G.; Stepanov, N.; Yurchenko, N.; Panina, E.; Zherebtsov, S.; Salishchev, G.; Stepanov, N. Oxidation Behavior of Refractory AlNbTiVZr0.25 High-Entropy Alloy. *Materials* **2018**, *11*, 2526. [CrossRef]
9. He, J.; Tang, Y.; Zhang, Z.; Li, S.; Zhu, L.; Ye, Y.; Luo, H.; Bai, S. Component Fluctuation and Lattice Distortion-Controlled Oxidation Behavior of Refractory Complex Concentrated Alloys. *Corros. Sci.* **2022**, *209*, 110778. [CrossRef]
10. Xu, T.; Chen, Q.; Ji, L.; Wang, H.; Qu, S.; Feng, A. Thermal Stability and Oxidation Resistance of Non-Equimolar Ratio AlTiVCrNb Refractory High-Entropy Alloys. *Intermetallics* **2023**, *160*, 107942. [CrossRef]
11. Lo, K.C.; Chang, Y.J.; Murakami, H.; Yeh, J.W.; Yeh, A.C. An Oxidation Resistant Refractory High Entropy Alloy Protected by CrTaO 4 -Based Oxide. *Sci. Rep.* **2019**, *9*, 7266. [CrossRef] [PubMed]
12. Gorr, B.; Müller, F.; Schellert, S.; Christ, H.-J.; Chen, H.; Kauffmann, A.; Heilmaier, M. A New Strategy to Intrinsically Protect Refractory Metal Based Alloys at Ultra High Temperatures. *Corros. Sci.* **2020**, *166*, 108475. [CrossRef]
13. Lo, K.C.; Murakami, H.; Yeh, J.W.; Yeh, A.C. Oxidation Behaviour of a Novel Refractory High Entropy Alloy at Elevated Temperatures. *Intermetallics* **2020**, *119*, 106711. [CrossRef]
14. Müller, F.; Gorr, B.; Christ, H.J.; Müller, J.; Butz, B.; Chen, H.; Kauffmann, A.; Heilmaier, M. On the Oxidation Mechanism of Refractory High Entropy Alloys. *Corros. Sci.* **2019**, *159*, 108161. [CrossRef]
15. Gorr, B.; Schellert, S.; Müller, F.; Christ, H.J.; Kauffmann, A.; Heilmaier, M. Current Status of Research on the Oxidation Behavior of Refractory High Entropy Alloys. *Adv. Eng. Mater.* **2021**, *23*, 2001047. [CrossRef]
16. Zhang, H.; Du, Y.; Lai, L.; Guo, N.; Li, N.; Guo, S. The As-Cast AlxCrTaTi Refractory Medium Entropy Alloys with Good Room-Temperature Mechanical Properties and High-Temperature Oxidation Resistance. *J. Alloys Compd.* **2023**, *932*, 167675. [CrossRef]
17. Butler, T.M.; Chaput, K.J.; Dietrich, J.R.; Senkov, O.N. High Temperature Oxidation Behaviors of Equimolar NbTiZrV and NbTiZrCr Refractory Complex Concentrated Alloys (RCCAs). *J. Alloys Compd.* **2017**, *729*, 1004–1019. [CrossRef]

18. Waseem, O.A.; Auyeskhan, U.; Lee, H.M.; Ryu, H.J. A Combinatorial Approach for the Synthesis and Analysis of AlxCry-MozNbTiZr High-Entropy Alloys: Oxidation Behavior. *J. Mater. Res.* **2018**, *33*, 3226–3234. [CrossRef]
19. Zhang, P.; Li, Y.; Chen, Z.; Zhang, J.; Shen, B. Oxidation Response of a Vacuum Arc Melted NbZrTiCrAl Refractory High Entropy Alloy at 800–1200 °C. *Vacuum* **2019**, *162*, 20–27. [CrossRef]
20. Gawel, R.; Rogal, L.; Przybylski, K. Oxidation Resistance of Ti-Al-Cr-Nb-Based High-Entropy Alloys in Air at 1073 K. *J. Mater. Eng. Perform.* **2019**, *28*, 4163–4170. [CrossRef]
21. Waseem, O.A.; Ryu, H.J. Combinatorial Synthesis and Analysis of Al_xTa_yVz-$Cr_{20}Mo_{20}Nb_{20}Ti20Zr_{10}$ and $Al_{10}CrMo_xNbTiZr_{10}$ Refractory High-Entropy Alloys: Oxidation Behavior. *J. Alloys Compd.* **2020**, *828*, 154427. [CrossRef]
22. Liu, C.Y.; Ma, Z.L.; Li, H.Y.; Xu, Z.Q.; Cheng, X.W. Designing NbTiTa-Cr/Al Refractory Complex Concentrated Alloys with Balanced Strength-Ductility-Oxidation Resistance Properties: Insights into Oxidation Mechanisms. *Int. J. Refract. Met. Hard Mater.* **2023**, *115*, 106308. [CrossRef]
23. Jayaraj, J.; Thirathipviwat, P.; Han, J.; Gebert, A. Microstructure, Mechanical and Thermal Oxidation Behavior of AlNbTiZr High Entropy Alloy. *Intermetallics* **2018**, *100*, 9–19. [CrossRef]
24. Butler, T.M.; Chaput, K.J. Native Oxidation Resistance of $Al_{20}Nb_{30}Ta_{10}Ti_{30}Zr_{10}$ Refractory Complex Concentrated Alloy (RCCA). *J. Alloys Compd.* **2019**, *787*, 606–617. [CrossRef]
25. Gorr, B.; Azim, M.; Christ, H.J.; Mueller, T.; Schliephake, D.; Heilmaier, M. Phase Equilibria, Microstructure, and High Temperature Oxidation Resistance of Novel Refractory High-Entropy Alloys. *J. Alloys Compd.* **2015**, *624*, 270–278. [CrossRef]
26. Gorr, B.; Mueller, F.; Christ, H.-J.; Mueller, T.; Chen, H.; Kauffmann, A.; Heilmaier, M. High Temperature Oxidation Behavior of an Equimolar Refractory Metal-Based Alloy 20Nb20Mo20Cr20Ti20Al with and without Si Addition. *J. Alloys Compd.* **2016**, *688*, 468–477. [CrossRef]
27. Gorr, B.; Müller, F.; Azim, M.; Christ, H.-J.; Müller, T.; Chen, H.; Kauffmann, A.; Heilmaier, M. High-Temperature Oxidation Behavior of Refractory High-Entropy Alloys: Effect of Alloy Composition. *Oxid. Met.* **2017**, *88*, 339–349. [CrossRef]
28. Sheikh, S.; Gan, L.; Ikeda, A.; Murakami, H.; Guo, S. Alloying Effect on the Oxidation Behavior of a Ductile $Al_{0.5}Cr_{0.25}Nb_{0.5}Ta_{0.5}Ti_{1.5}$ Refractory High-Entropy Alloy. *Mater. Today Adv.* **2020**, *7*, 100104. [CrossRef]
29. Ostovari Moghaddam, A.; Sudarikov, M.; Shaburova, N.; Zherebtsov, D.; Zhivulin, V.; Ashurali Solizoda, I.; Starikov, A.; Veselkov, S.; Samoilova, O.; Trofimov, E. High Temperature Oxidation Resistance of W-Containing High Entropy Alloys. *J. Alloys Compd.* **2022**, *897*, 162733. [CrossRef]
30. Lowell, C.E.; Deadmore, D.L. The Role of Thermal Shock in Cyclic Oxidation. *Oxid. Met.* **1980**, *14*, 325–336. [CrossRef]
31. Yurchenko, N.; Panina, E.; Zherebtsov, S.; Stepanov, N. Oxidation Behaviour of Eutectic Refractory High-Entropy Alloys at 800–1000 °C. *Corros. Sci.* **2022**, *205*, 110464. [CrossRef]
32. Panina, E.S.; Yurchenko, N.Y.; Zherebtsov, S.V.; Tikhonovsky, M.A.; Mishunin, M.V.; Stepanov, N.D. Structures and Mechanical Properties of Ti-Nb-Cr-V-Ni-Al Refractory High Entropy Alloys. *Mater. Sci. Eng. A* **2020**, *786*, 139409. [CrossRef]
33. Zhang, H.; Zhao, Y.; Cai, J.; Ji, S.; Geng, J.; Sun, X.; Li, D. High-Strength NbMoTaX Refractory High-Entropy Alloy with Low Stacking Fault Energy Eutectic Phase via Laser Additive Manufacturing. *Mater. Des.* **2021**, *201*, 109462. [CrossRef]
34. Yurchenko, N.; Panina, E.; Shaysultanov, D.; Zherebtsov, S.; Stepanov, N. Refractory High Entropy Alloy with Ductile Intermetallic B2 Matrix/Hard Bcc Particles and Exceptional Strain Hardening Capacity. *Materialia* **2021**, *20*, 101225. [CrossRef]
35. Yurchenko, N.; Panina, E.; Rogal, Ł.; Shekhawat, L.; Zherebtsov, S.; Stepanov, N. Unique Precipitations in a Novel Refractory Nb-Mo-Ti-Co High-Entropy Superalloy. *Mater. Res. Lett.* **2022**, *10*, 78–87. [CrossRef]
36. Panina, E.; Yurchenko, N.; Tojibaev, A.; Mishunin, M.; Zherebtsov, S.; Stepanov, N. Mechanical Properties of $(HfCo)_{100-x}(NbMo)_x$ Refractory High-Entropy Alloys with a Dual-Phase Bcc-B2 Structure. *J. Alloys Compd.* **2022**, *927*, 167013. [CrossRef]
37. Xiao, B.; Jia, W.; Wang, J.; Zhou, L. Selective Electron Beam Melting of WMoTaNbVFeCoCrNi Refractory High-Entropy Alloy. *Mater. Charact.* **2022**, *193*, 112278. [CrossRef]
38. Zhang, H.; Cai, J.; Geng, J.; Sun, X.; Zhao, Y.; Guo, X.; Li, D. Study on Annealing Treatment of NbMoTaTiNi High-Entropy Alloy with Ultra-High Strength Disordered-Ordered Transition Structure for Additive Manufacturing. *J. Alloys Compd.* **2023**, *941*, 168810. [CrossRef]
39. Zhang, H.; Cai, J.; Geng, J.; Sun, X.; Zhao, Y.; Guo, X.; Li, D. Development of High Strength High Plasticity Refractory High Entropy Alloy Based on Mo Element Optimization and Advanced Forming Process. *Int. J. Refract. Met. Hard Mater.* **2023**, *112*, 106163. [CrossRef]
40. Panina, E.; Yurchenko, N.; Salishchev, G.; Zherebtsov, S.; Stepanov, N. Thermal Stability of $(HfCo)_{90}(NbMo)_{10}$ and $(HfCo)_{75}(NbMo)_{25}$ Refractory High Entropy Alloys with a Bcc + B2 Structure. *Int. J. Refract. Met. Hard Mater.* **2023**, *115*, 106297. [CrossRef]
41. Soni, V.; Gwalani, B.; Senkov, O.N.; Viswanathan, B.; Alam, T.; Miracle, D.B.; Banerjee, R. Phase Stability as a Function of Temperature in a Refractory High-Entropy Alloy. *J. Mater. Res.* **2018**, *33*, 3235–3246. [CrossRef]
42. Soni, V.; Senkov, O.N.; Couzinie, J.-P.; Zheng, Y.; Gwalani, B.; Banerjee, R. Phase Stability and Microstructure Evolution in a Ductile Refractory High Entropy Alloy $Al_{10}Nb_{15}Ta_5Ti_{30}Zr_{40}$. *Materialia* **2020**, *9*, 100569. [CrossRef]
43. Whitfield, T.E.; Pickering, E.J.; Owen, L.R.; Jones, C.N.; Stone, H.J.; Jones, N.G. The Effect of Al on the Formation and Stability of a BCC—B2 Microstructure in a Refractory Metal High Entropy Superalloy System. *Materialia* **2020**, *13*, 100858. [CrossRef]
44. Whitfield, T.E.; Pickering, E.J.; Owen, L.R.; Senkov, O.N.; Miracle, D.B.; Stone, H.J.; Jones, N.G. An Assessment of the Thermal Stability of Refractory High Entropy Superalloys. *J. Alloys Compd.* **2021**, *857*, 157583. [CrossRef]

45. Whitfield, T.E.; Church, N.L.; Stone, H.J.; Jones, N.G. On the Rate of Microstructural Degradation of Al-Ta-Ti-Zr Refractory Metal High Entropy Superalloys. *J. Alloys Compd.* **2023**, *939*, 168369. [CrossRef]
46. Birks, N.; Meier, G.; Pettit, F. *Introduction to the High Temperature Oxidation of Metals*, 2nd ed.; Cambridge University Press: Cambridge, UK, 2006; ISBN 9781139163903.
47. HfO2 Crystal Structure—SpringerMaterials. Available online: https://materials.springer.com/isp/crystallographic/docs/sd_0313894 (accessed on 21 July 2023).
48. HfO2 Crystal Structure—SpringerMaterials. Available online: https://materials.springer.com/isp/crystallographic/docs/sd_0310050 (accessed on 21 July 2023).
49. CoO Crystal Structure—SpringerMaterials. Available online: https://materials.springer.com/isp/crystallographic/docs/sd_0307718 (accessed on 21 July 2023).
50. Nb2Co4O9 Crystal Structure—SpringerMaterials. Available online: https://materials.springer.com/isp/crystallographic/docs/sd_0556980 (accessed on 21 July 2023).
51. MoO3 Crystal Structure—SpringerMaterials. Available online: https://materials.springer.com/isp/crystallographic/docs/sd_0530932 (accessed on 21 July 2023).
52. Robertson, J.; Manning, M.I. Limits to Adherence of Oxide Scales. *Mater. Sci. Technol.* **1990**, *6*, 81–92. [CrossRef]
53. Schütze, M. Mechanical Aspects of High-Temperature Oxidation. *Corros. Sci.* **1993**, *35*, 955–963. [CrossRef]
54. Chan, K.S. A Mechanics-Based Approach to Cyclic Oxidation. *Metall. Mater. Trans.* **1997**, *28*, 411–422. [CrossRef]
55. Su, R.; Zhang, H.; Ouyang, G.; Liu, L.; Nachlas, W.; Cui, J.; Johnson, D.D.; Perepezko, J.H. Enhanced Oxidation Resistance of $(Mo_{95}W_5)_{85}Ta_{10}(TiZr)_5$ Refractory Multi-Principal Element Alloy up to 1300 °C. *Acta Mater.* **2021**, *215*, 117114. [CrossRef]
56. Müller, F.; Gorr, B.; Christ, H.J.; Chen, H.; Kauffmann, A.; Heilmaier, M. Effect of Microalloying with Silicon on High Temperature Oxidation Resistance of Novel Refractory High-Entropy Alloy Ta-Mo-Cr-Ti-Al. *Mater. High Temp.* **2018**, *35*, 168–176. [CrossRef]
57. Senkov, O.N.; Daboiku, T.; Butler, T.M.; Rao, S.I.; Payton, E.J. Microstructure, Compression Properties, and Oxidation Behavior of Hf-25Ta-5Me Alloys (Me Is Mo, Nb, W, 0.5Mo + 0.5 W, Cr, or Zr). *Int. J. Refract. Met. Hard Mater.* **2022**, *109*, 105968. [CrossRef]
58. Ouyang, D.; Chen, Z.; Yu, H.; Chan, K.C.; Liu, L. Oxidation Behavior of the $Ti_{38}V_{15}Nb_{23}Hf_{24}$ Refractory High-Entropy Alloy at Elevated Temperatures. *Corros. Sci.* **2022**, *198*, 110153. [CrossRef]
59. Lo, K.-C.; Murakami, H.; Glatzel, U.; Yeh, J.-W.; Gorsse, S.; Yeh, A.-C. Elemental Effects on the Oxidation of Refractory Compositionally Complex Alloys. *Int. J. Refract. Met. Hard Mater.* **2022**, *108*, 105918. [CrossRef]
60. Zhang, R.; Meng, J.; Han, J.; Tulugan, K.; Zhang, R. Oxidation Resistance Properties of Refractory High-Entropy Alloys with Varied AlxCrTiMo Content. *J. Mater. Sci.* **2021**, *56*, 3551–3561. [CrossRef]

Disclaimer/Publisher's Note: The statements, opinions and data contained in all publications are solely those of the individual author(s) and contributor(s) and not of MDPI and/or the editor(s). MDPI and/or the editor(s) disclaim responsibility for any injury to people or property resulting from any ideas, methods, instructions or products referred to in the content.